JOURNAL OF SYNCHROTRON RADIATION
ISSN 1600-5775

Current status of the TwinMic beamline at Elettra: a soft X-ray transmission and emission microscopy station

Alessandra Gianoncelli,* George Kourousias, Lucia Merolle, Matteo Altissimo and Anna Bianco

Elettra – Sincrotrone Trieste, SS 14, Km in Area Science Park, Basovizza, Trieste 34149, Italy.
*Correspondence e-mail: alessandra.gianoncelli@elettra.eu

Received 19 February 2016
Accepted 10 September 2016

Edited by I. Schlichting, Max Planck Institute for Medical Research, Germany

Keywords: X-ray microscopy; X-ray fluorescence; STXM; full-field imaging; soft X-rays.

The current status of the TwinMic beamline at Elettra synchrotron light source, that hosts the European twin X-ray microscopy station, is reported. The X-ray source, provided by a short hybrid undulator with source size and divergence intermediate between bending magnets and conventional undulators, is energy-tailored using a collimated plane-grating monochromator. The TwinMic spectromicroscopy experimental station combines scanning and full-field imaging in a single instrument, with contrast modes such as absorption, differential phase, interference and darkfield. The implementation of coherent diffractive imaging modalities and ptychography is ongoing. Typically, scanning transmission X-ray microscopy images are simultaneously collected in transmission and differential phase contrast and can be complemented by chemical and elemental analysis using across-absorption-edge imaging, X-ray absorption near-edge structure or low-energy X-ray fluorescence. The lateral resolutions depend on the particular imaging and contrast mode chosen. The TwinMic range of applications covers diverse research fields such as biology, biochemistry, medicine, pharmacology, environment, geochemistry, food, agriculture and materials science. They will be illustrated in the paper with representative results.

1. Introduction

The unique capability of X-ray microscopes to explore heterogeneous phenomena at microscopic length scales has a steadily increasing impact in micro-characterization of solid and liquid matter, as demonstrated by the growing number of X-ray microscopy instruments worldwide (Howells *et al.*, 2006). The two typical X-ray microscopy configurations used are transmission X-ray microscopy (TXM) and scanning transmission X-ray microscopy (STXM). In STXM imaging mode the specimen is raster-scanned across an X-ray microprobe, while emitted and transmitted signals can be simultaneously acquired by suitable detection systems, making this imaging mode preferable for elemental mapping and chemical analysis (Kirz *et al.*, 1992). On the other hand, morphological studies with fast single-shot imaging for dynamics and microtomography are typically performed by TXM where the X-ray light is condensed onto the specimen and an objective lens magnifies in transmission the specimen onto a two-dimensional detector (Schmahl *et al.*, 1993).

Zeitler's reciprocity principle of microscopy (Zeitler & Thomson, 1970), which expresses the interchangeability of source and detector roles in microscopes, inspired a consortium of scientists from several European and associated countries to systematically integrate the advantages of both available microscope types, STXM and TXM, into a single

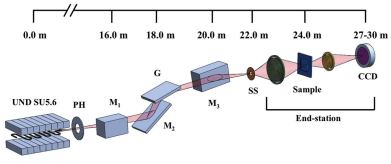

© 2016 International Union of Crystallography

instrument in the frame of the EC FP5 project 'TwinMic', which was developed under contract number HPRI-CT-2001-50024 (Kaulich *et al.*, 2006).

While STXM requires spatially coherent illumination, partial coherence or incoherent illumination is preferred for TXM (Jochum & Meyer-Ilse, 1995). Thus STXM instruments are typically installed at undulator sources (McNulty *et al.*, 1995; Nilsson *et al.*, 2005; Susini *et al.*, 2002; Winn *et al.*, 2000) and TXM instruments at bending magnets (Meyer-Ilse *et al.*, 1998; Medenwaldt & Uggerhoj, 1998; Niemann *et al.*, 1994), although *vice versa* setups have been reported (Kaulich *et al.*, 1999; Kilcoyne *et al.*, 2003; Guttmann *et al.*, 2001). The X-ray spectromicroscopy beamline (see Fig. 1) we describe here is optimized for operating both in STXM and TXM by using a short hybrid undulator with intermediate source and divergence properties as compared with bending-magnet and conventional undulator sources. This paper describes the overall features and capabilities of the TwinMic beamline, aiming at becoming a reference for the TwinMic user community. An early paper (Kaulich *et al.*, 2006) describes the features and capabilities of the early end-station, built and designed between 2001 and 2004, and temporarily installed at the BACH beamline (Zangrando *et al.*, 2004) in Elettra. The current TwinMic beamline was built in 2006 and the microscope end-station was moved and installed there in 2007. Several papers were published later on, describing various upgrades of the instrument, such as the LEXRF system (Gianoncelli *et al.*, 2009, 2013*a*, 2016*a*) and/or the imaging capabilities of TwinMic microscope (Kaulich *et al.*, 2009; Gianoncelli *et al.*, 2016*b*). However, at present there is no paper describing extensively and exhaustively the whole TwinMic beamline and the current end-station layout and performances: the aim of the present work is to cover this gap.

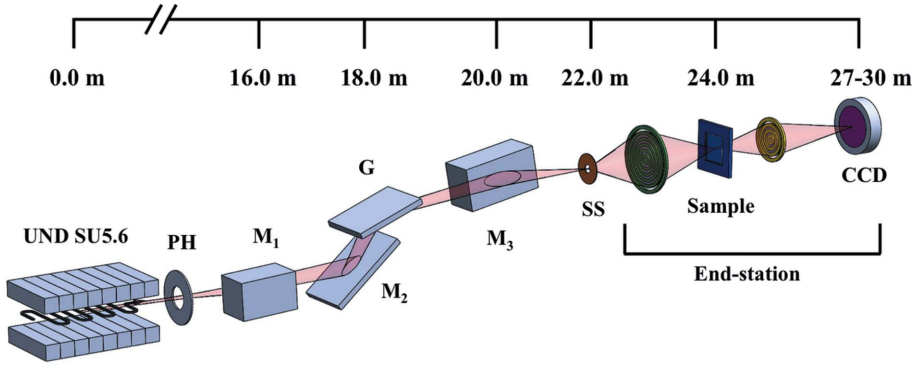

Figure 1
Optical scheme of the TwinMic beamline with short undulator X-ray source (SU5.6), pinhole (PH), collimating cylindrical mirror (M_1), plane-grating monochromator [plane mirror (M_2) and plane grating (G)], refocusing toroidal mirror (M_3) and secondary X-ray source (SS). The TwinMic microscope end-station, comprising zone plates, sample and CCD is indicated, and will be described in detail in §3.

2. General beamline layout

Fig. 1 presents the general beamline and optical layout. The X-ray beam generated by the undulator is collimated by a vertically arranged cylindrical mirror into a plane-grating monochromator in order to adapt photon flux and energy resolution to the experimental requirements. A toroidal mirror refocuses the beam into a secondary source, which consists of an array apertures (with diameter 15, 25, 35, 50, 75 100 or 150 µm) serving as exit slit and defining the monochromaticity of the beam delivered into the end-station, as illustrated in Fig. 1.

2.1. Short hybrid undulator SU5.6

The limited number of long straight sections (11 in total) of the Elettra storage ring led in 1998 to the installation of a 1 m short undulator with 56 mm period (SU5.6) in one of the shortest dispersive straight sections (Diviacco *et al.*, 1994). Table 1 reports the spatial and angular dimensions of the electron beam at the centre of the insertion device for the two electron storage ring energies, 2 and 2.4 GeV. Elettra operates at 2 GeV electron energy and 310 mA storage ring current for 75% of its user-dedicated time, and at 2.4 GeV and 160 mA for the remaining user-dedicated time. This dual operation mode of the storage ring is due to a historical choice, taken during the commissioning of Elettra in order to favor the hard X-ray beamlines at 2.4 GeV (Karantzoulis, 2016). The undulator has 17 periods and a minimum gap value of 25 mm, corresponding to a maximum magnetic field of 0.5 T. The emitted radiation has a spatial FWHM size of 724 µm (h) × 51 µm (v) and FWHM angular divergence of 171 µrad (h) × 88 µrad (v) at 400 eV photon energy and 2 GeV electron energy, which correspond to a horizontal and vertical phase-space area of about 124 nm rad and 5 nm rad, respectively. The working photon energy range, 400–2200 eV, is covered by the first, third and fifth harmonics of SU5.6, as shown in Fig. 2.

Table 1
Electron beam spatial and angular dimensions for the two operating electron energies, 2 and 2.4 GeV, in the centre of the 1.1 straight section where the SU5.6 undulator is installed.

Electron energy (GeV)	Electron beam spatial size $\sigma_h \times \sigma_v$ (µm)	Electron beam angular size $\sigma'_h \times \sigma'_v$ (µrad)
2.0	327.3 × 22.0	66.2 × 5.6
2.4	453.6 × 25.7	85.3 × 6.6

The energy range of the beamline can in principle be extended to about 3.5 keV with the storage ring in 2.4 GeV operation mode and using higher undulator harmonics. Fig. 3 shows a SU5.6 spectrum acquired at the minimum 25 mm gap with a calibrated photodiode after a 100 µm secondary X-ray source, SS. The measured peak flux of 1×10^{12} photons s^{-1} $(100\ mA)^{-1}$ corresponds to the peak flux in the plane of the first microprobe forming zone plate (ZP), about 2 mm^2 FWHM.

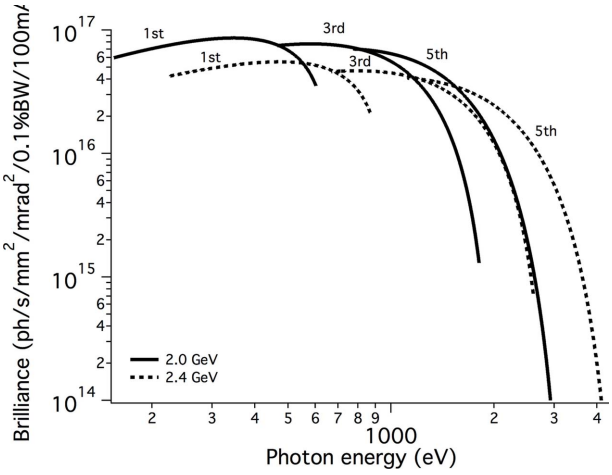

Figure 2
Expected brilliance of the SU5.6 short undulator in first, third and fifth harmonics. Brilliance data are calculated using the code *Spectra* (Tanaka & Kitamura, 2001) for 2.0 and 2.4 GeV operation mode of the synchrotron; data are normalized to 100 mA beam current. Each curve has been evaluated varying the gap from the minimum allowed value of 25 mm, which corresponds to the minimum photon energy for each harmonic.

One of the major disadvantages of using a short straight section is the lack of space for electron beam position monitors, which would be used to control the beam trajectory at the entrance and exit of SU5.6. Therefore, two X-ray beam position monitors control the beam stability. The first is a conventional four-blade tungsten monitor in 45° configuration developed at BESSY (Holldack *et al.*, 2001) and is located at around 6.2 m from the undulator. A second beam position monitor, 6.4 m downstream, consists of two raster-scannable apertures (indicated as PH in Fig. 1), 1 mm and 0.1 mm in diameter, separated by 3.3 mm, and allows the X-ray beam trajectory to be followed in terms of position and angle.

2.2. Beamline optics

The design of the beamline preconditioning optics has been dictated by preserving as much as possible the efficiency over the entire photon energy range. This is accomplished by simple, fast and highly reproducible alignment procedures from low to high photon energies, together with stigmatic demagnification into the secondary source.

Table 2
Description of the energy-filtering array located upstream of the toroidal mirror.

Metallic filter	Thickness (μm)	Support (μm)	Coating (nm)
Mg	0.2	Si_3N_4 0.1	Au 50
Mn	0.06	Si_3N_4 0.1	
Al	3	Foil	
Cu	0.22	Si_3N_4 0.1	
Ni	0.15	Si_3N_4 0.1	
Co	0.5	Si_3N_4 0.075	
Fe	0.15	Si_3N_4 0.1	
Ti	0.09	Si_3N_4 0.05	Au 50

The Au-coated water-cooled cylindrical mirror (M_1) with a sagittal radius of curvature ρ = 56 cm is mounted 16 m from the source at 1° grazing incidence. It separates bremsstrahlung and higher photon energies, absorbing about 60% of the incident power. The cylindrical mirror focuses the beam into a collimated plane-grating monochromator (PGM) (Naletto & Tondello, 1992; Follath *et al.*, 1998) equipped with two 600 lines mm^{-1} Au gratings with blazed angles of 1.1° (G1 grating) and 0.4° (G2 grating), optimized for the 150–1500 eV and 1000–4000 eV energy ranges, respectively (Bianco *et al.*, 2005; Cocco *et al.*, 2007). The energy-resolving power of the PGM is reported in Fig. 4 for different secondary source diameters, under typical working conditions, *i.e.* first internal order and two constant values for the included angle. The latter is set to 175.44° and 177.17°, respectively, for the 400–900 eV [low-energy (LE)] and the 900–2200 eV [high-energy (HE)] energy range. The grating's angular positions are optimized for high flux rather than higher harmonics rejection, which is accomplished by an energy-filtering array, consisting of different metal foils (Table 2) located just upstream of the toroidal mirror (M_3).

The Au-coated toroidal mirror (M_3) has tangential and sagittal radii of curvature R = 211 m and ρ = 6.7 cm, respectively. The mirror is located 20 m downstream of the source and generates the stigmatic focus, which acts as a secondary source for the microscope, by demagnifying the primary X-ray source ten times in the horizontal and eight times in the vertical plane. Table 3 summarizes the main characteristics of

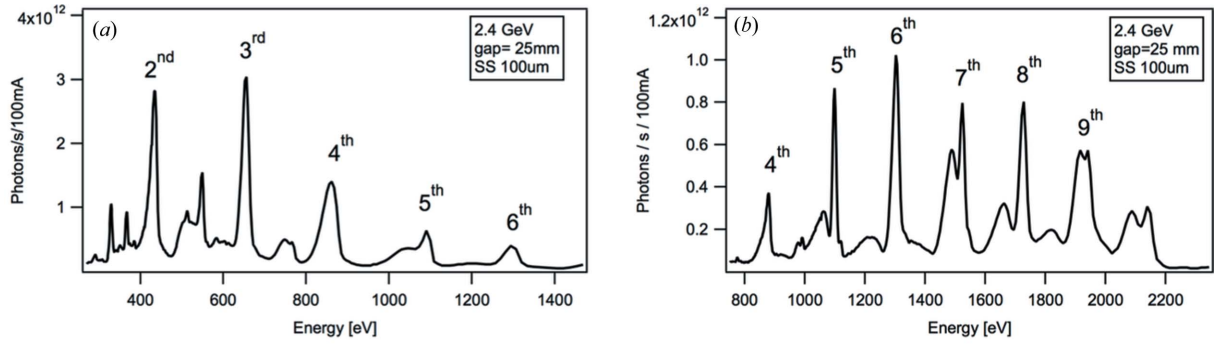

Figure 3
(*a*) SU5.6 spectrum acquired in low-energy configuration (PGM mirror incidence angle at 2.28°) with a minimum undulator gap of 25 mm after a 100 μm-diameter aperture acting as SS. The photon flux corresponds to the flux in an area of about 2 mm^2 FHWM on the plane of the first focusing optic of the TwinMic end-station. (*b*) SU5.6 spectrum acquired in high-energy configuration (PGM mirror angle at 1.41°) with the same parameters.

Table 3
Parameters of the optical elements.

Optical element	Collimating mirror M_1	Plane mirror M_2	Plane grating G_1 and G_2	Focusing mirror M_3
Shape	Cylinder	Plane	Plane	Toroid
Deflection	Horizontal	Vertical	Vertical	Horizontal
Grazing incidence angle	1°	Variable	Variable	1°
Source distance (mm)	16000	Variable	18000	20000
Dimensions (mm)				
Blank (L × W × H)	160 × 30 × 30	600 × 50 × 60	100 × 20 × 30	160 × 30 × 42
Active area (L × W)	100 × 5	580 × 10	80 × 6	100 × 5
Coating	Gold	Gold	Gold	Gold
Tangential radius (m)	>20000†	>20000†	>20000†	211†
Sagittal radius (m)	0.56†	–	–	0.067†
Groove density (lines mm^{-1})	–	–	600‡	–
Surface roughness RMS (nm)	<0.3†		0.3†	0.1†
Groove shape			Blazed	
Blaze angle			γ_1 = 1.1°‡, γ_2 = 0.4°†	

† Measured at Elettra soft X-ray laboratory (Cocco *et al.*, 2005). ‡ Nominal value.

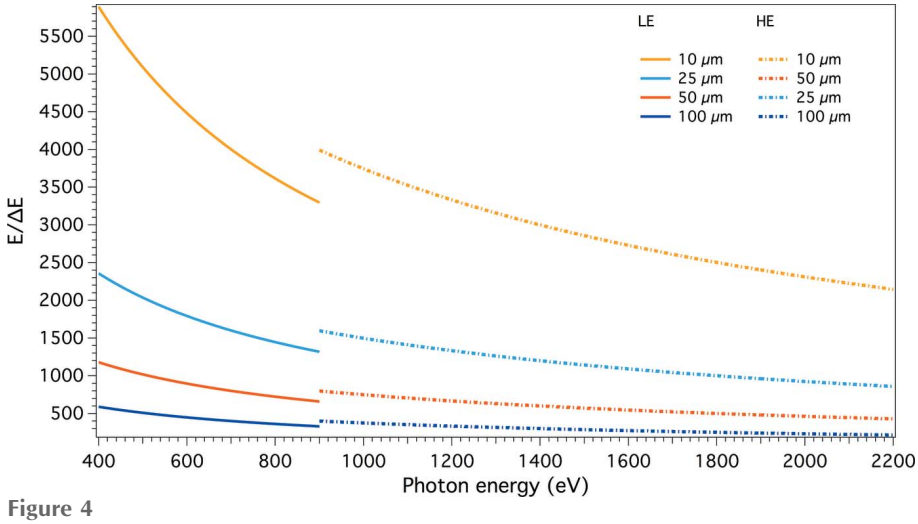

Figure 4
Calculated contribution of the SS diameter to the resolving power for typical working conditions. LE: low-energy configuration; HE: high-energy configuration. Sizes refer to the SS diameter.

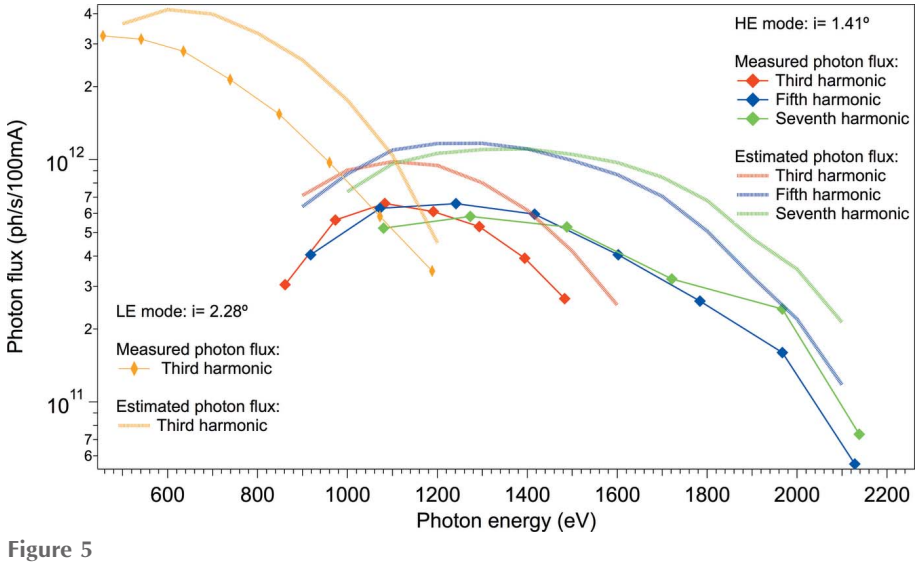

Figure 5
Calculated and measured photon flux through a 100 μm-diameter SS. The grating G_1 has been used in the two operational modes, low-energy and high-energy. Data are normalized to 100 mA electron current, the electron energy is 2 GeV.

all the optical elements. Ray-tracing calculations show that with the 1 mm pinhole, 12.6 m from the source, at 400 eV photon energy the stigmatic spot is about 76 μm (h) × 4 μm (v) FWHM with a divergence of 0.6 mrad (h) × 1.8 mrad (v). This corresponds to a horizontal and vertical phase-space area of about 46 nm rad and 7 nm rad, respectively. Thus a 500 μm-diameter ZP at 1.5–2 m downstream is easily overfilled due to the significant beam divergence from this SS.

The SS is effected by a set of circular apertures (15, 25, 35, 50, 75, 100 or 150 μm in diameter) in the STXM's backfocal plane of M_3, and so define the source size or phase-space area for diffraction-limited operation of the microscope in STXM mode, or can be used to tune the delivered photon flux.

An estimation of the photon flux at the entrance of the microscope (SS; see Fig. 1) has been performed calculating the expected photon flux emitted by the undulator within the angular acceptance of the beamline, the reflectivities of the (idealized) mirrors, the efficiency of the (idealized) grating and the resolving power of the monochromator due to the SS aperture. Fig. 5 summarizes the simulated and measured photon flux through a 100 μm-diameter SS as a function of photon energy. An agreement within a factor of two was obtained, which is satisfactory given the assumptions detailed above as well as accumulated contamination of the optical surfaces.

It is worth noting that the monochromaticity provided by the beamline is typically not sufficient for diffraction-limited focusing with ZPs but the problem can be overcome by using the ZP itself with a small aperture as monochromatizing element (Niemann *et al.*, 1974). The achievable lateral resolution of the microscope is mainly limited by the optical properties of diffractive optics, which are for example concisely described and summarized by Attwood (2007). In STXM mode, the lateral resolution δ is a Gaussian convolution of the diffraction-limited resolution δ_d, the geometrical resolution given by the geometrical demagnification δ_g and a chromatic aberration factor δ_c (Yun *et al.*, 1999):

$$\delta_d = 1.22\Delta r_N, \qquad \delta_g = SS_{size}(f/L), \qquad \delta_c = D(\Delta E/E), \tag{1}$$

where Δr_N is the outermost zone width of the ZP, SS_{size} is the secondary source diameter, f is the first-order focal length of the ZP, L is the SS–ZP distance (about 2.2 m in the case of TwinMic), D is the ZP diameter and $\Delta E/E$ is the degree of monochromaticity of the beam. Each contribution is then summed in quadrature to obtain the spot size δ:

$$\delta = \left(\delta_d^2 + \delta_g^2 + \delta_c^2\right)^{1/2}. \tag{2}$$

For a 250 µm-diameter and 80 nm outermost zone width ZP, the diffraction-limited resolution is δ_d = 98 nm. For 500 eV photon energy and a secondary source size of 10 µm diameter, the geometrical demagnification contributes with δ_g = 40 nm and the chromatic aberrations give δ_c = 26 nm, whereas at 1500 eV photon energy δ_g = 121 nm and δ_c = 45 nm (see Fig. 6).

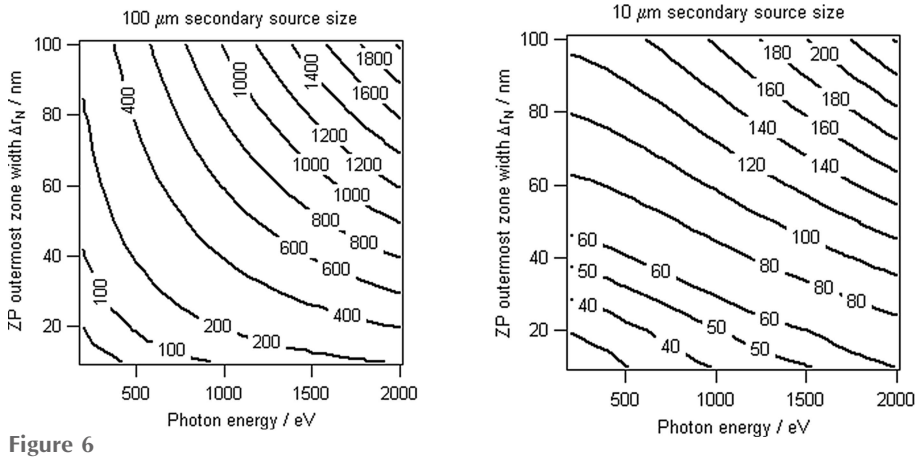

Figure 6
Spatial resolution achievable in TwinMic STXM mode *versus* the outermost zone width of a 200 µm-diameter ZP and the photon energy. A SS–ZP distance of 2.2 m and the energy resolutions of the PGM from Fig. 4 have been considered. The labels indicate the lateral resolution in nm.

3. TwinMic end-station

The TwinMic instrument has been designed to address a broad spectrum of applications ranging from life, earth and environmental sciences to food and agriculture, sustainable energies, nanotechnologies and new materials. Therefore, rather than focusing on ultimate spatial resolution, the microscope's conceptual design focuses on integrating the versatility of different imaging modes (*i.e.* STXM and TXM) in a single instrument with a manifold of contrast techniques and spectroscopies. The experimental chamber was designed to perform correlative measurements with other microscopies. The sample environment is modular, and can in principle be operated in air, inert gas atmosphere or vacuum (typically high vacuum, reaching down to around 10^{-6} mbar), and it is therefore adaptable to many scientific applications.

3.1. STXM operation mode

In STXM mode, a ZP focuses the incoming photon beam, and the specimen is raster-scanned across the microprobe as shown in Fig. 7. An order-sorting aperture (OSA) is placed downstream of the ZP to discriminate unwanted diffraction orders, while a central stop on the ZP absorbs most of the zeroth-order radiation. Since each scan typically includes a few tens of thousands of pixels, a fast read-out transmission detection system is essential.

While single-element detectors add essentially no delay, it was recognized early on that more sophisticated detection schemes allow complementary information to be acquired such as phase contrast or darkfield (Morrison & Browne, 1992; Feser *et al.*, 2006; Hornberger *et al.*, 2008; Vogt *et al.*, 2001).

Phase-sensitive imaging in such complementary modes is facilitated by configured detectors (Morrison & Niemann,

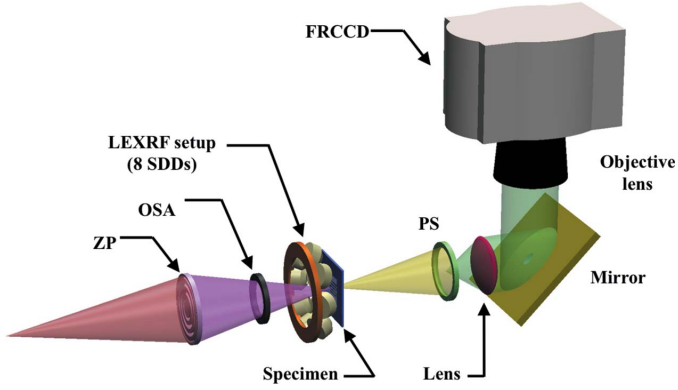

Figure 7
STXM mode as implemented on TwinMic: the beam is focused by a microprobe forming zone plate (ZP), and a combination of a central stop (not shown in the figure) and an order-sorting aperture (OSA) transmits only the desired diffracted light onto the specimen. The detection system collects the transmitted photons with a fast-readout CCD (FRCCD) camera through a visible-light-converting system constituted by a phosphor screen (PS), a first lens (Lens), a 45° inclined mirror (Mirror) and an objective lens. A low-energy X-ray fluorescence (LEXRF setup) detector system is also present in slightly backscattering configuration.

1996) that determine the phase gradient of the specimen by measuring the shift of the illumination in the detector plane.

3.1.1. Fast-readout transmission CCD detector. The TwinMic setup uses an Andor Ixon DV860-BV electron-multiplied fast-readout CCD (FRCCD) camera (Coates *et al.*, 2003), where the effective response of each CCD pixel is software configurable. The FRCCD camera has 128 × 128 pixels with 24 µm × 24 µm pixel size. The CCD chip is back-side thinned and could be used for direct X-ray detection, but the most flexible solution for the 400–2200 eV photon energy range makes use of a visible-light-converting system (VLCS), since the electron-multiplying electronics provide excellent sensitivity and low-noise operation for visible light. The VLCS used on TwinMic consists of a folded-path configuration with a Gd_2O_2S:Tb (P43) phosphor screen (PS) and high-numerical-aperture lenses (*F*-number of 1 or 1.2). The expected efficiency of the light-converting system is 2% with an *F*-number of 1.2, and 4% with $F = 1.0$ (Gianoncelli *et al.*, 2006). The FRCCD detector system allows simultaneous acquisition of absorption and differential phase contrast imaging, with online display during acquisition, and is potentially suited for ptychographic imaging (Rodenburg *et al.*, 2007; Thibault *et al.*, 2008) if the contributions from scattered light in the image maps by the VLCS can be reduced.

A major drawback of the FRCCD system is its low VLCS conversion efficiency (about 4%), which is currently limiting the dwell time per pixel to about 10 ms. This is in general accepted by having the different contrast maps online available during the acquisition without need of post-processing, sequential acquisition of different maps with changing optics or applying phase contrast techniques as reported by Kaulich *et al.* (2002).

The transmitted X-ray signals collected by the CCD allow determining the morphology of the specimen and mapping the elemental and chemical distribution by means of across-absorption-edge imaging (AAEI) (Jacobsen *et al.*, 2000) or examination of the X-ray absorption near-edge spectroscopy (XANES). Both modes require scanning the photon energy and refining the focal length of diffractive focusing optics, which is optomechanically demanding and sometimes time-consuming, especially if the photon energy has to be changed over a wide range.

3.1.2. Low-energy X-ray fluorescence system. Characteristic X-ray fluorescence lines are emitted by a sample when the latter is illuminated by a primary X-ray beam. The detection of the emitted fluorescent photons provides simultaneous information of all elemental constituents that can be excited by the primary X-ray beam (Jenkins *et al.*, 1995; Janssens *et al.*, 2000). Several setups have been described in the past performing low-energy X-ray fluorescence (Jia *et al.*, 1995; Stuik *et al.*, 1999). The LEXRF system implemented on the TwinMic end-station consists of eight silicon drift detectors (SDDs) mounted circularly around the specimen (see Fig. 7). Each of the SDD detectors has an active area of 30 mm^2 and the acceptance solid angle subtended by the single SDD collimator is $\Omega = 3 \times 10^{-2}$ sterad. The measured FWHM energy resolution is 69 eV at the C *Kα* line as shown in Fig. 8, and

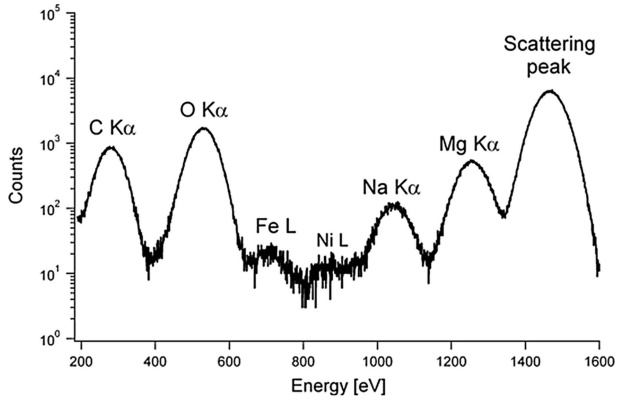

Figure 8
LEXRF spectrum of a section of a book page treated with a polymer containing Mg, acquired with four SDD detectors with a 440 nm-diameter spot size. The primary photon energy (scattering peak) is 1468 eV. Acquisition time of the whole spectrum is 300 s, with an average count rate of 4 kcounts s^{-1}.

87 eV at the Na *Kα* line for count rates up to 30 kcounts s^{-1} (Alberti *et al.*, 2009; Gianoncelli *et al.*, 2009, 2013*a*). The customized read-out electronic boards are based on a pulsed reset preamplifier (Niculae *et al.*, 2006) and a field programmable gate array (FPGA) setup (Alberti *et al.*, 2008).

3.1.3. Absorption spectroscopy with the TwinMic STXM mode. Even though the STXM system has not yet been optimized for XANES measurements, absorption spectroscopy can be performed either (i) by acquiring a stack of images across the absorption edge of specific chemical elements (Jacobsen *et al.*, 2000) or (ii) by collecting an absorption spectrum with a photodiode downstream of the sample, as shown for instance by Bozzini *et al.* (2010, 2014) and Gianoncelli *et al.* (2011). XANES measurements in fluorescence mode are about to be tested and developed, and we expect no significant issues in realising this modality.

3.1.4. Examples of research with the TwinMic STXM mode. The STXM operation mode of the TwinMic microscope has attracted the interest of a broad spectrum of users' communities and has been successfully used in different research fields from fuel cell technology, biotechnology, biomaterials, food science and nanotoxicology, neuroscience to clinical medicine. Recent results in the life science field include new insights into (i) the morphology distribution and correlation of chemical elements during plant growth under various environmental conditions and in the presence of toxic substances (Tolrà *et al.*, 2011; Regvar *et al.*, 2011), (ii) concentration dependence of penetration of magnetic nanoparticles in different cell organelles and changes in the nanoparticle chemistry inside the cells (Marmorato *et al.*, 2011; Gianoncelli *et al.*, 2013*b*), (iii) cellular internalization and degradation of magnetic nanoparticles in digestive gland epithelium (Novak *et al.*, 2013), (iv) reaction of lung tissue to the presence of inhaled asbestos fibres (Pascolo *et al.*, 2011, 2013), (v) glucose metabolism and uptake in neurons and glial cells (Poitry-Yamate *et al.*, 2013), and many others. In this paper we report two examples of on-going related researches

illustrating the potential of TwinMic STXM mode in relevant research domains.

The first example concerns a long-term collaboration with the Electrochemical Material Science Group of Salento University (Lecce, Italy) where soft X-ray spectromicroscopy has been used for electrochemical applications related to fuel cells and batteries fields (Bozzini *et al.*, 2012, 2013). Fig. 9(*a*) shows the corner of a Ni electrode after galvanic corrosion in the presence of Nafion, a sulfonated tetrafluoroethylene-based polymer. The C and F lateral distribution allows the Nafion flakes to be located. The elemental maps show the presence of Ni only inside the electrode region, whereas O seems to be present in both the Ni and Nafion areas. The Ni chemical state was investigated measuring the Ni L_3 spectra at the indicated points inside the electrode, showing some degree of lateral inhomogeneity in the thickness of the NiO passivating layer (Bozzini *et al.*, 2010). The reported experiment was conducted under *in situ* operation conditions after developing vacuum-compatible electrochemical cells, suitable for soft X-ray applications.

The second example shows on-going nanotoxicology-related research focused on the study of the effects of magnetic nanoparticles on cells. In particular, the investigation concerns Balb3T3 mouse fibroblast cells grown on Si_3N_4 windows exposed for 24 h to different concentrations (from 40 to 1000 µM) of $CoFe_2O_4$ nanoparticles (NPs) (50 nm average diameter) and chemically fixed after 24 h with PFA 4% (Marmorato *et al.*, 2011). Fig. 9(*b*) shows the absorption and differential phase contrast images together with the elemental map of C, O, Fe and Co of a cell exposed to a 1000 µ*M* concentration of $CoFe_2O_4$ NPs. The maps were acquired at 0.92 keV excitation energy, with 500 nm lateral resolution. Beside the information about NPs location given by the Fe and Co spatial distribution, the absorption and phase contrast images provide insight on how the cell morphology changes under a NP-related stress. In particular, as already reported

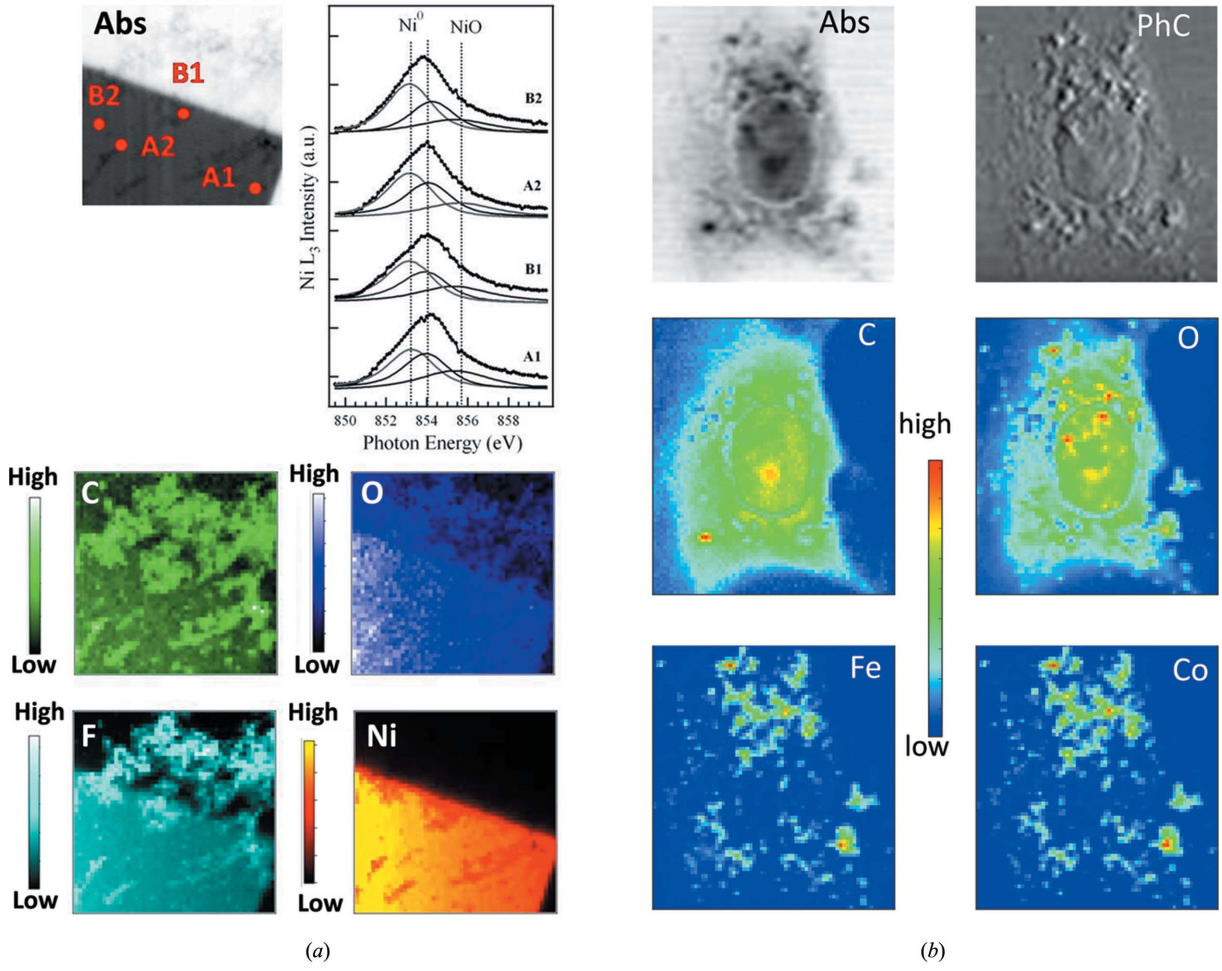

Figure 9
(*a*) Absorption (Abs) image of a Ni electrode together with the elemental distribution of C, O, F and Ni (1 keV excitation energy, with a spot size of 1 µm^2 over an area of 80 µm × 80 µm), and XANES spectra acquired at the points indicated in panel Abs. The acquisition times were 5 s pixel^{-1} for LEXRF and 20 ms for the absorption image. The XANES spectra were collected point by point with a photodiode downstream of the sample for an overall acquisition time of ∼15 min. (*b*) Absorption (Abs) and differential phase contrast images (PhC) together with the elemental distribution of C, O, Fe and Co of a mouse fibroblast cell exposed to a 1000 µ*M* concentration of $CoFe_2O_4$ nanoparticles. Data acquired with 920 eV excitation energy, 500 nm spot size, 5 s pixel^{-1} acquisition time for LEXRF and 200 ms pixel^{-1} for STXM images. The image area is 35 µm × 40 µm.

(Marmorato *et al.*, 2011; Gianoncelli *et al.*, 2013*b*), a high concentration of NPs causes the development of a white corona around the cell nucleus. Although it has not yet been investigated, this phenomenon could be ascribed to a defence mechanism of the cells against the toxic effect of the high dose of the xenobiotic on the DNA.

3.2. TXM operation mode

A TXM operates similar to a visible-light transmission microscope. A condenser illuminates the specimen and an objective lens magnifies the specimen onto a CCD detector (see Fig. 10). On TwinMic, the TXM is mostly operated in brightfield contrast mode. An adaptation of X-ray differential interference contrast (Kaulich, Wilhein *et al.*, 2002; Wilhein *et al.*, 2001) to soft X-rays and the relative implementation are currently under development. The adoption of Zernike phase contrast remains as an option for a future upgrade development.

Operation of a TXM at an undulator source requires a special specimen illumination scheme to adapt the spatial coherence (Jochum & Meyer-Ilse, 1995). The TwinMic condenser is an unconventional beam-shaping diffractive focusing optic consisting of a large number of concentrically arranged linear gratings with different line widths, producing a nearly homogeneous Koehler-type intensity distribution on the specimen plane (Jefimovs *et al.*, 2008; Vogt *et al.*, 2006). The CBS (condenser beam shaper) used is 1 mm in diameter and consists of 256 grating elements arranged on five rings. The grating constants are 218 nm and 126 nm for the innermost and outermost rings, respectively. Each grating covers an area of 50 µm × 50 µm. The CBS was fabricated by zoneplates.com. A wire of 150 µm diameter is glued on the CBS holder and acts as a central stop.

3.2.1. TXM detection scheme. A back-illuminated slow-scan CCD camera (Princeton) with 1300 × 1340 pixels and a pixel size of 20 µm × 20 µm is used for operation in the 400–900 eV photon energy range (LECCD). A second back-illuminated Princeton AT200L slow-scan CCD camera with 1024 × 1024 pixels and a pixel size of 24 µm × 24 µm is coupled to a folded-path VLCS and can be operated in the 700–2200 eV region without any risk of radiation damage of the CCD chip. The VLCS consists of Gd_2O_2S:Tb phosphor screen with a thickness of 10 µm and grain size of 7 µm FWHM. The two-stage optical system has a numerical aperture of 1.8 and gives a 3.14× optical magnification (Salomé *et al.*, 1999). The two CCD cameras can be exchanged by manual translations. The optical magnification and the object field size can be adapted by varying the distance of the detector to the specimen from 0.7 to 4 m. Thus, using an objective zone plate (OZP) with a focal length of f = 4 mm, M can be varied from 1000× to 175× providing object fields from 30 µm up to 175 µm on the sample plane, and a best-case scenario resolution of about 20–120 nm, respectively.

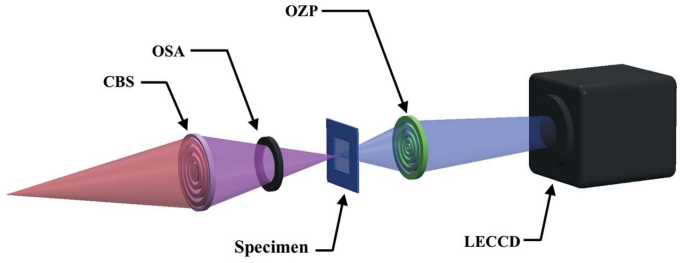

Figure 10
Transmission X-ray microscopy (TXM) mode as implemented in the TwinMic station with a condenser beamshaper (CBS) illuminating the specimen, an order-sorting aperture (OSA), an objective zone plate (OZP) that magnifies the image of the specimen into the detector with a directly illuminated CCD camera (LECCD) for < 900 eV photon energies and a similar camera system (HECCD) adapted to a folded-path high-numerical-aperture visible-light-converting system (VLCS) developed at the ESRF (Salomé *et al.*, 1999).

3.2.2. TXM imaging performance. The TXM imaging performance is demonstrated by imaging a Ni Siemens star, 20 µm in diameter, with 60 spokes and thus 525 nm outermost structures and innermost structures of about 30 nm. The Siemens star was fabricated by BIOX, KTH Stockholm, Sweden (http://www.electrumlab.se/KTHAcreo.aspx). The test object was imaged at 720 eV photon energy with a Ni OZP having a diameter of 110 µm and 50 nm outermost zones. The OZP was fabricated by TASC/INFM, Trieste, Italy. A diffraction-limited resolution of about 60 nm has been achieved (Fig. 11*a*).

By using a zone-doubled OZP (Vila-Comamala *et al.*, 2009) with a diameter of 100 µm and 15 nm outermost zone width a diffraction-limited resolution of about 20 nm was achieved (Fig. 11*b*). Fig. 12 shows two typical TwinMic life-science applications: a TXM brightfield image of (*a*) a wheat grain, highlighting the presence of globoids in starches from wheat grains (Regvar *et al.*, 2011) and (*b*) an asbestos body in a lung tissue (Pascolo *et al.*, 2013). A comparison between STXM and TXM modes has been given by Gianoncelli *et al.* (2016*a*).

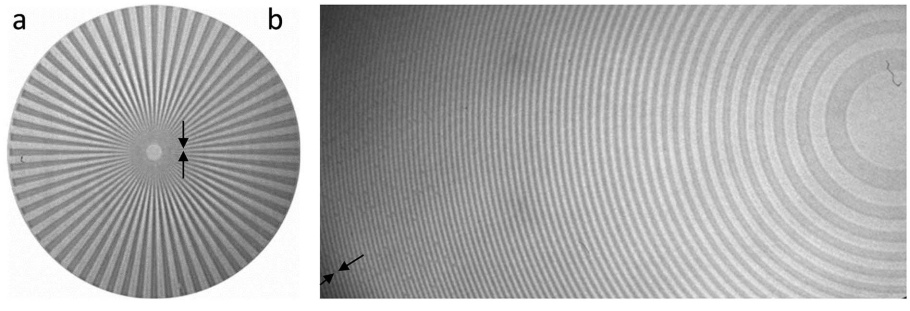

Figure 11
(*a*) X-ray micrograph of a Siemens star test pattern in Ni with 20 µm diameter and 60 spokes. The test pattern was imaged with an OZP, 110 µm in diameter and 50 nm outermost zone width. Smallest features of about 60 nm can be resolved (arrows). (*b*) X-ray micrograph of a zone plate in Au. The test pattern was imaged with a zone-doubled OZP, 100 µm in diameter and 15 nm outermost zone width. A photon energy of 720 eV and an acquisition time of 10 s were used for both. Smallest features of about 20 nm can be resolved (arrows).

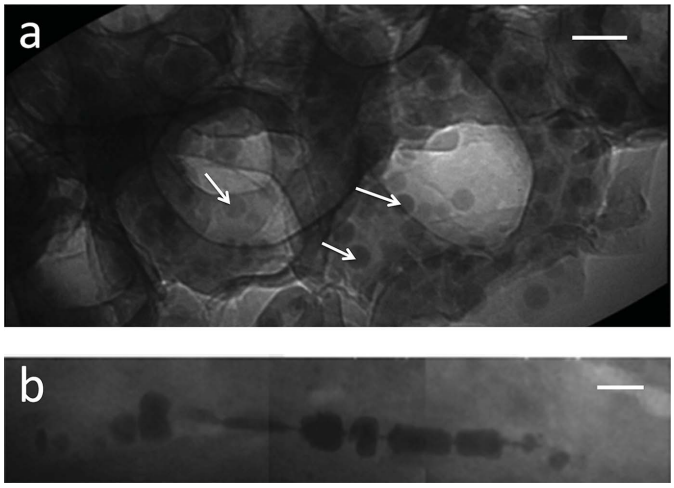

Figure 12
X-ray micrographs of globoids structures (arrows) in the aleurone layer of a wheat grain (10 µm-thick cryosectioned slide) (*a*) and an asbestos body in a paraffinated lung tissue section (5 µm thick) (*b*) acquired at 707 eV with a zone-doubled ZP (Vila-Comamala *et al.*, 2009) with 5 s acquisition time per frame. Scale bars: 5 µm.

3.3. CDI operation mode

Thanks to the flexibility and modularity of the TwinMic design, additional imaging modes such as coherent diffractive imaging (CDI) can be performed at the TwinMic end-station.

A further imaging opportunity has been recently demonstrated by performing soft X-ray spectromicroscopy using ptychography with a randomly phased illumination. The proof of principle has been illustrated by acquiring scans across the *L*-absorption edge of iron on fibroblast cells exposed to cobalt ferrite nanoparticles (Maiden *et al.*, 2013). Furthermore, phase-diverse Fresnel CDI (fCDI) has been successfully used for the first time in the water window on malaria parasite-infected red blood cells to reveal their cellular architecture (Jones *et al.*, 2013).

Fig. 13 shows absorption and phase images of a test object and a section of a tomato stem acquired at 1.02 keV through fCDI ptychography. The monochromatised microprobe beam was delivered by a 600 µm-diameter ZP with a 50 nm outermost zone width and 140 µm-diameter central stop. The sample was placed at around 480 µm downstream of the focus, providing a round illuminated area of about 12.5 µm diameter on the sample plane. Both samples were raster scanned with a step size of 4 µm across the microprobe over a raster scan of 6 × 6 positions with an acquisition time of 1.5 s frame^{-1}. The images were collected by the same 1300 × 1340 pixel Princeton CCD camera used in TXM mode, in this case placed at around 75.5 cm from the focal spot. As can be seen from Fig. 13, one of the advantages of ptychography is the possibility of quantitatively reconstructing both amplitude and phase with a spatial resolution much higher than the probe size. In particular, by using a probe size of around 12.5 µm in diameter we were able to detect the 100 nm features of the linear grating shown in Figs. 13(*a*) and 13(*b*). The shown reconstructions feature artefacts and imperfections but reflect the current status of the implemented technique. Ptychography is a field with a very active development. There is continued progress and its results are being gradually implemented in the workflow of the beamline. This should allow for faster acquisitions and better image reconstructions. The current focus of the ptychography workflow is on developing an efficient setup for using the CDI method for monitoring dynamic processes (Kourousias *et al.*, 2016).

4. Ongoing upgrades

4.1. Control system upgrade

The computer systems facilitating the control of the beamline are of crucial importance in modern laboratories. Such systems consist of specialized hardware and software, and are used for beamline and end-station control, as well as

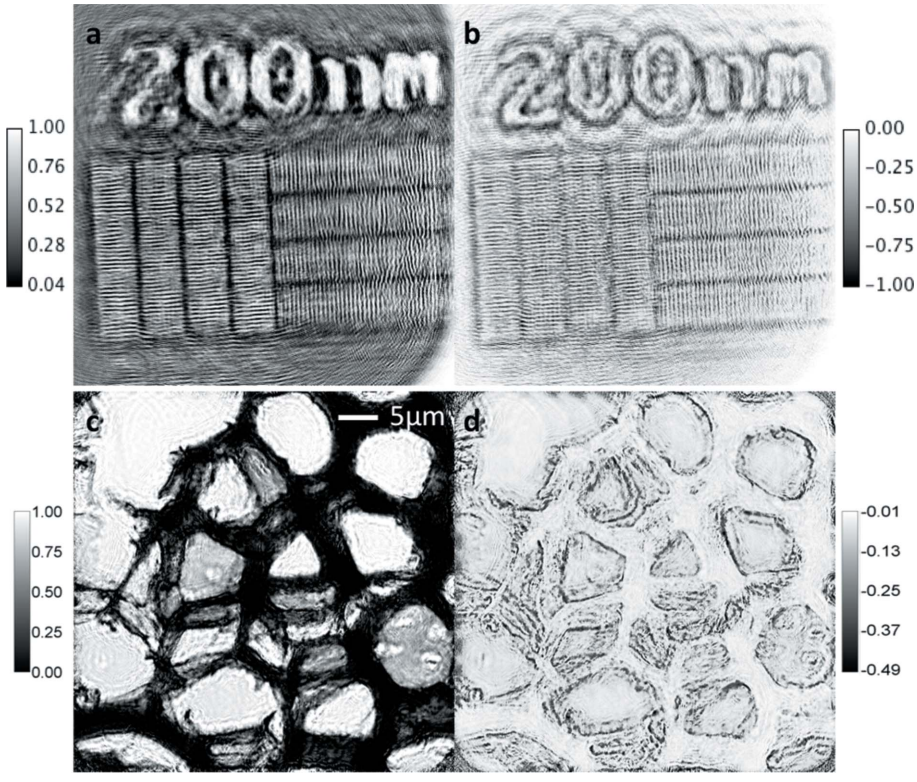

Figure 13
Absorption (*a*, *c*) and phase (*b*, *d*) images of a test object (*a*, *b*) and a 7 µm-thick section of a tomato stem (*c*, *d*), both acquired at 1.02 keV through fCDI ptychography. The periodicity of the linear grating was 200 nm.

data acquisition during the experiments. The initial control solution for TwinMic was based on NI LabView under Windows, controlling multiple motors, pumps and detectors. The latest TwinMic upgrades and experimental needs demanded an improved control system. For the past year, a new control system has been under development, providing high reliability, easy inclusion of new instruments and rapid hosting of custom experimental requirements. The new control system is in gradual deployment in parallel to the original one thus achieving minimum downtime. Developed in-house and using the experience from the highly demanding beamlines of the free-electron laser FERMI@ELETTRA, the Elettra Scientific Computing Team has based the system on the Tango distributed control system under Linux (Borghes *et al.*, 2013), using open-source software. Full use of virtualization technologies is in place for both the control devices and the user interface allowing for reliability but also for easy remote control of the experiments. Advanced HDF5-based data formats are planned for all the spectroscopy and imaging techniques while the system allows for access to on- and off-site dedicated computing resources for data analysis. Facilitating easy experiment control with integrated data acquisition, management and analysis is of high importance in computational-demanding techniques like ptychography.

4.2. LEXRF system

The small portion of the emission solid angle collected by the current TwinMic LEXRF detector system coupled with the intrinsically low fluorescence yields for photon energies below 2 keV require the use of acquisition times of a few second per pixel. This translates into long measurement times (of the order of several hours) and higher radiation damage to the specimen. A recent collaboration between Elettra and several other Italian institutions resulted in the on-going development of a new LEXRF detector system that aims at providing improved solid-angle coverage. It is based on the use of four trapezoidal chips, each containing six to eight SDDs, the signal of which is processed by a new electronic chain system (Gianoncelli *et al.*, 2016*b*). This system is scheduled for full commissioning in December 2017.

5. Summary, conclusion and outlook

We described a multi-purpose X-ray transmission and emission microscopy beamline operating in the 400–2200 eV photon energy range that merges the advantages of STXM (simultaneous multi-detector acquisition and chemical sensitivity) with TXM (fast one-shot data acquisition optimized morphological studies and dynamics) into a single instrument. Versatile contrast mechanisms such as brightfield, phase-sensitive and chemical contrast modes are implemented in both imaging modes, facilitating the experimentalist to adapt the measurements to specific requirements, highlighted by the implementation of LEXRF. The strategy to design a broad-band versatile X-ray microscopy instrument with versatility in imaging options rather than concentrating on higher lateral resolution and lower probing depth has been welcomed by the users of the instrument. Around 4 h are typically needed to switch from one modality to the other one, and this can be done during a typical user beam time. Nonetheless, it is a rare occurrence, since the users prefer to focus their experiments on a single modality per beam time. The TwinMic beamline is open to users for 70% of Elettra's storage ring users' operation time, and routinely addresses applications from biology, biochemistry and medicine (∼50%), geochemistry, environmental and food science (∼20%), cultural heritage (∼10%) and RT&D (∼7%). There is a steadily growing number of experiments correlated to other synchrotron-based techniques, such as infrared microscopy and medical imaging at Elettra, as well as laboratory techniques. The large amount of life sciences requests and correlative research makes the extension to cryogenic cooling of the specimen environment a high-priority topic. Further, in order to better respond to the increasing life sciences demands, a more efficient LEXRF detector system is being developed. This will be coupled with a more precise sample stage, able to accommodate a larger number of samples, which is currently being designed. Also, a new Tango-based beamline control system is being developed and deployed in order to improve the overall usability and accessibility. Furthermore, high-resolution imaging modalities such as CDI and ptychography are about to become standard operation modes available also to non-specialist users.

Besides providing users' support and advanced imaging capabilities, thanks to its unique flexibility and modularity, the TwinMic beamline is also involved in new imaging detector developments and characterization (Wunderer *et al.*, 2015). Recent efforts have also been made to create a synergy with the new DiProI microscopy beamline at the FERMI FEL accelerator (Trieste, Italy) (Pedersoli *et al.*, 2011) regarding the possibility to perform combined experiments on both microscopy beamlines. The scope is performing experiments where measurements using different sources and techniques can be combined (*e.g.* synchrotron LEXRF with FEL CDI).

Acknowledgements

We acknowledge Burkhard Kaulich (Diamond Light Source, UK) for the scientific conception of TwinMic, the steering of its construction and commissioning (in the frame of the EU project contract number HPRI-CT-2001-50024) and for running the beamline as scientific coordinator until 2011. Daniele Cocco (SLAC National Accelerator Laboratory, USA) is acknowledged for the design and commissioning of the beam transport and monochromatizing optics. The authors express their appreciation to Maya Kiskinova (Elettra – Sincrotrone Trieste, Italy) for her support and fundamental contributions to the X-ray microscopy scientific programs at Elettra. The results shown in Figs. 9, 12 and 13 were obtained in collaboration with Benedetto Bozzini (University of Salento, Lecce, Italy), Giacomo Ceccone (Joint Research Centre, Institute for Health and Consumer Protection, Ispra, Italy), Lorella Pascolo (University of Trieste, Italy), Ivan Kreft (University of Ljubljana, Slovenia), Irene Rosellini (ISE-CNR

Pisa, Italy) and Martina Puccinelli (DAFE, University of Pisa, Italy). We thank Diego Lonza (Elettra – Sincrotrone Trieste, Italy), Andrea Stolfa (Elettra – Sincrotrone Trieste, Italy) and the Elettra Scientific Computing team for their precious technical support in the construction and running of the beamline.

References

Alberti, R., Guazzoni, C. & Klatka, T. (2008). *J. Instrum.* **3**, P03003.

Alberti, R., Klatka, T., Bacescu, D., Marcello, A., De Marco, A., Gianoncelli, A., Kaulich, B. & Longoni, A. (2009). *X-ray Spectrom.* **38**, 205–209.

Attwood, D. (2007). *Soft X-rays and Extreme Ultraviolet Radiation: Principles and Applications.* Cambridge University Press.

Bianco, A., Sostero, G., Nelles, B., Heidemann, K. F. & Cocco, D. (2005). *Proc. SPIE*, **5918**, 591810.

Borghes, R., Chenda, V., Curri, A., Kourousias, G., Lonza, M., Prica, M. & Pugliese, R. (2013). *Proceedings of ICALEPCS2013*, San Francisco, CA, USA, pp. 6–11.

Bozzini, B., Abyaneh, M. K., Amati, M., Gianoncelli, A., Gregoratti, L., Kaulich, B. & Kiskinova, M. (2012). *Chem. Eur. J.* **18**, 10196–10210.

Bozzini, B., Amati, M., Gianoncelli, A., Gregoratti, L., Kaulich, B. & Kiskinova, M. (2013). *J. Phys. Conf. Ser.* **463**, 012018.

Bozzini, B., Gianoncelli, A., Bocchetta, P., Dal Zilio, S. & Kourousias, G. (2014). *Anal. Chem.* **86**, 664–670.

Bozzini, B., Gianoncelli, A., Kaulich, B., Kiskinova, M., Prasciolu, M. & Sgura, I. (2010). *ChemSusChem*, **3**, 846–850.

Coates, C. G., Denvir, D. J., Hollywood, M. A., McHale, N. G., Thornbury, K. D. & Hollywood, M. A. (2003). *Proc. SPIE*, **5139**, 56–66.

Cocco, D., Bianco, A., Kaulich, B., Schaefers, F., Mertin, M., Reichardt, G., Nelles, B. & Heidemann, K. F. (2007). *AIP Conf. Proc.* **879**, 497–500.

Cocco, D., Bianco, A. & Sostero, G. (2005). *Proc. SPIE*, **5921**, 59210L.

Diviacco, B., Bracco, R., Codutti, A., Millo, D., Walker, R. P. & Zangrando, D. (1994). *4th European Particle Accelerator Conference*, London, UK, p. 2250.

Feser, M., Hornberger, B., Jacobsen, C., De Geronimo, G., Rehak, P., Holl, P. & Strüder, L. (2006). *Nucl. Instrum. Methods Phys. Res. A*, **565**, 841–854.

Follath, R., Senf, F. & Gudat, W. (1998). *J. Synchrotron Rad.* **5**, 769–771.

Gianoncelli, A., Bufon, J., Ahangarianabhari, M., Altissimo, M., Bellutti, P., Bertuccio, G., Borghes, R., Carrato, S., Cautero, G., Fabiani, S., Giacomini, G., Giuressi, D., Kourousias, G., Menk, R. H., Picciotto, A., Piemonte, C., Rachevski, A., Rashevskaya, I., Stolfa, A., Vacchi, A., Zampa, G., Zampa, N. & Zorzi, N. (2016*b*). *Nucl. Instrum. Methods Phys. Res. A*, **816**, 113–118.

Gianoncelli, A., Kaulich, B., Alberti, R., Klatka, T., Longoni, A., de Marco, A., Marcello, A. & Kiskinova, M. (2009). *Nucl. Instrum. Methods Phys. Res. A*, **608**, 195–198.

Gianoncelli, A., Kaulich, B., Kiskinova, M., Prasciolu, M., D'Urzo, B. & Bozzini, B. (2011). *Micron*, **42**, 342–347.

Gianoncelli, A., Kourousias, G., Altissimo, M., Bedolla, D., Merolle, L., Stolfa, A. & Shin, H.-J. (2016*a*). *AIP Conf. Proc.* **1764**, 030002.

Gianoncelli, A., Kourousias, G., Stolfa, A. & Kaulich, B. (2013*a*). *J. Phys. Conf. Ser.* **425**, 182001.

Gianoncelli, A., Marmorato, P., Ponti, J., Pascolo, L., Kaulich, B., Uboldi, C., Rossi, F., Makovec, D., Kiskinova, M. & Ceccone, G. (2013*b*). *X-ray Spectrom.* **42**, 316–320.

Gianoncelli, A., Morrison, G. R., Kaulich, B., Bacescu, D. & Kovac, J. (2006). *Appl. Phys. Lett.* **89**, 251117.

Guttmann, P., Niemann, B., Thieme, J., Hambach, D., Schneider, G., Wiesemann, U., Rudolph, D. & Schmahl, G. (2001). *Nucl. Instrum. Methods Phys. Res. A*, **467–468**, 849–852.

Holldack, K., Ponwitz, D. & Peatman, W. B. (2001). *Nucl. Instrum. Methods Phys. Res. A*, **467–468**, 213–220.

Hornberger, B., de Jonge, M. D., Feser, M., Holl, P., Holzner, C., Jacobsen, C., Legnini, D., Paterson, D., Rehak, P., Strüder, L. & Vogt, S. (2008). *J. Synchrotron Rad.* **15**, 355–362.

Howells, M., Jacobsen, C. & Warwick, A. (2006)., *Science of Microscopy*, Vols. 1–2, edited by P. W. Hawkes and J. C. H. Spence, pp. 1–91. Heidelberg: Springer.

Jacobsen, C., Wirick, S., Flynn, G. & Zimba, C. (2000). *J. Microsc.* **197**, 173–184.

Janssens, K., Adams, F. & Rindby, A. (2000). *Microscopic X-ray Fluorescence Analysis.* New York: Wiley.

Jefimovs, K., Vila-Comamala, J., Stampanoni, M., Kaulich, B. & David, C. (2008). *J. Synchrotron Rad.* **15**, 106–108.

Jenkins, R., Gould, R. W. & Gedcke, D. (1995). *Quantitative X-ray Spectrometry.* New York: M. Dekker.

Jia, J. J., Callcott, T. A., Yurkas, J., Ellis, A. W., Himpsel, F. J., Samant, M. G., Stöhr, J., Ederer, D. L., Carlisle, J. A., Hudson, E. A., Terminello, L. J., Shuh, D. K. & Perera, R. C. C. (1995). *Rev. Sci. Instrum.* **66**, 1394–1397.

Jochum, L. & Meyer-Ilse, W. (1995). *Appl. Opt.* **34**, 4944–4950.

Jones, M. W., Abbey, B., Gianoncelli, A., Balaur, E., Millet, C., Luu, M. B., Coughlan, H. D., Carroll, A. J., Peele, A. G., Tilley, L. & van Riessen, G. A. (2013). *Opt. Express*, **21**, 32151–32159.

Karantzoulis, E. (2016). *Synchrotron Radiat. News*, **29**, 29–33.

Kaulich, B., Gianoncelli, A., Beran, A., Eichert, D., Kreft, I., Pongrac, P., Regvar, M., Vogel-Mikus, K. & Kiskinova, M. (2009). *J. R. Soc. Interface*, **6**, S641–S647.

Kaulich, B., Oestreich, S., Salome, M., Barrett, R., Susini, J., Wilhein, T., Di Fabrizio, E., Gentili, M. & Charalambous, P. (1999). *Appl. Phys. Lett.* **75**, 4061–4063.

Kaulich, B., Polack, F., Neuhaeusler, U., Susini, J., di Fabrizio, E. & Wilhein, T. (2002). *Opt. Express*, **10**, 1111–1117.

Kaulich, B., Susini, J., David, C., Di Fabrizio, E., Morrison, G., Charalambous, P., Thieme, J., Wilhein, T., Kovac, J., Bacescu, D., Salome, J. M., Dhez, O., Weitkamp, T., Cabrini, S., Cojoc, D., Gianoncelli, A., Vogt, U., Podnar, M., Zangrando, M., Zacchigna, M. & Kiskinova, M. (2006). *X-ray Microscopy 2005*, edited by S. Aoki, Y. Kagoshima and I. H. Suzuki, pp. 377–379. Himeji: IPAP.

Kaulich, B., Wilhein, T., Di Fabrizio, E., Romanato, F., Altissimo, M., Cabrini, S., Fayard, B. & Susini, J. (2002). *J. Opt. Soc. Am. A*, **19**, 797–806.

Kilcoyne, A. L. D., Tyliszczak, T., Steele, W. F., Fakra, S., Hitchcock, P., Franck, K., Anderson, E., Harteneck, B., Rightor, E. G., Mitchell, G. E., Hitchcock, A. P., Yang, L., Warwick, T. & Ade, H. (2003). *J. Synchrotron Rad.* **10**, 125–136.

Kirz, J., Ade, H., Jacobsen, C., Ko, C. H., Lindaas, S., McNulty, I., Sayre, D., Williams, S., Zhang, X. & Howells, M. (1992). *Rev. Sci. Instrum.* **63**, 557–563.

Kourousias, G., Bozzini, B., Gianoncelli, A., Jones, M. W. M., Junker, M., van Riessen, G. & Kiskinova, M. (2016). *Nano Res.* **9**, 2046–2056.

McNulty, I., Haddad, W. S., Trebes, J. E. & Anderson, E. H. (1995). *Rev. Sci. Instrum.* **66**, 1431–1433.

Maiden, A., Morrison, G. R., Kaulich, B., Gianoncelli, A. & Rodenburg, J. (2013). *Nat. Commun.* **4**, 1669.

Marmorato, P., Ceccone, G., Gianoncelli, A., Pascolo, L., Ponti, J., Rossi, F., Salomé, M., Kaulich, B. & Kiskinova, M. (2011). *Toxicol. Lett.* **207**, 128–136.

Medenwaldt, R. & Uggerhoj, E. (1998). *Rev. Sci. Instrum.* **69**, 2974–2977.

Meyer-Ilse, W., Medecki, H., Brown, J. T., Heck, J. M., Anderson, E., Stead, A., Ford, T., Balhorn, R., Petersen, C., Magowan, C. & Attwood, D. (1998). *X-ray Microscopy and Spectromicroscopy*, edited by J. Thieme, G. Schmahl, D. Rudolph and E. Umbach, p. I-3. Berlin: Springer Verlag.

Morrison, G. R. & Browne, M. T. (1992). *Rev. Sci. Instrum.* **63**, 611–614.

Morrison, G. R. & Niemann, B. (1996). *X-ray Microscopy and Spectromicroscopy*, edited by J. Thieme, D. Rudolph, G. Schmahl and E. Umbach, pp. I-85–I-94. Berlin: Springer Verlag.
Naletto, G. & Tondello, G. (1992). *Pure Appl. Opt.* **1**, 347–358.
Niculae, A., Lechner, P., Soltau, H., Lutz, G., Strüder, L., Fiorini, C. & Longoni, A. (2006). *Nucl. Instrum. Methods Phys. Res. A*, **568**, 336–342.
Niemann, B., Rudolph, D. & Schmahl, G. (1974). *Opt. Commun.* **12**, 160–163.
Niemann, B., Schneider, G., Guttmann, P., Rudolph, D. & Schmahl, G. (1994). *X-ray Microscopy IV*, edited by V. V. Aristov and A. Erko, pp. 66–75. Chernologovka: Bogorodskii Pechnatnik.
Nilsson, H. J., Tyliszczak, T., Wilson, R. E., Werme, L. & Shuh, D. K. (2005). *Anal. Bioanal. Chem.* **383**, 41–47.
Novak, S., Drobne, D., Golobič, M., Zupanc, J., Romih, T., Gianoncelli, A., Kiskinova, M., Kaulich, B., Pelicon, P., Vavpetič, P., Jeromel, L., Ogrinc, N. & Makovec, D. (2013). *Environ. Sci. Technol.* **47**, 5400–5408.
Pascolo, L., Gianoncelli, A., Kaulich, B., Rizzardi, C., Schneider, M., Bottin, C., Polentarutti, M., Kiskinova, M., Longoni, A. & Melato, M. (2011). *Part. Fibre Toxicol.* **8**, 7.
Pascolo, L., Gianoncelli, A., Schneider, G., Salomé, M., Schneider, M., Calligaro, C., Kiskinova, M., Melato, M. & Rizzardi, C. (2013). *Sci. Rep.* **3**, 1123.
Pedersoli, E., Capotondi, F., Cocco, D., Zangrando, M., Kaulich, B., Menk, R. H., Locatelli, A., Mentes, T. O., Spezzani, C., Sandrin, G., Bacescu, D. M., Kiskinova, M., Bajt, S., Barthelmess, M., Barty, A., Schulz, J., Gumprecht, L., Chapman, H. N., Nelson, A. J., Frank, M., Pivovaroff, M. J., Woods, B. W., Bogan, M. J. & Hajdu, J. (2011). *Rev. Sci. Instrum.* **82**, 043711.
Poitry-Yamate, C., Gianoncelli, A., Kaulich, B., Kourousias, G., Magill, A. W., Lepore, M., Gajdosik, V. & Gruetter, R. (2013). *J. Neurosci. Res.* **91**, 1050–1058.
Regvar, M., Eichert, D., Kaulich, B., Gianoncelli, A., Pongrac, P., Vogel-Mikus, K. & Kreft, I. (2011). *J. Exp. Bot.* **62**, 3929–3939.
Rodenburg, J. M., Hurst, A. C., Cullis, A. G., Dobson, B. R., Pfeiffer, F., Bunk, O., David, C., Jefimovs, K. & Johnson, I. (2007). *Phys. Rev. Lett.* **98**, 034801.
Salomé, M., Peyrin, F., Cloetens, P., Odet, C., Laval-Jeantet, A. M., Baruchel, J. & Spanne, P. (1999). *Med. Phys.* **26**, 2194–2204.
Schmahl, G., Rudolph, D., Niemann, B., Guttmann, P., Thieme, J., Schneider, G., David, C., Diehl, M. & Wilhein, T. (1993). *Optik* **93**, 95–102.
Stuik, R., Shmaenok, L. A., Fledderus, H., Andreev, S. S., Shamov, E. A., Zuev, S. Y., Salashchenko, N. N. & Bijkerk, F. (1999). *J. Anal. At. Spectrom.* **14**, 387–390.
Susini, J., SalomÉ, M., Fayard, B., Ortega, R. & Kaulich, B. (2002). *Surf. Rev. Lett.* **09**, 203–211.
Tanaka, T. & Kitamura, H. (2001). *J. Synchrotron Rad.* **8**, 1221–1228.
Thibault, P., Dierolf, M., Menzel, A., Bunk, O., David, C. & Pfeiffer, F. (2008). *Science*, **321**, 379–382.
Tolrà, R., Vogel-Mikuš, K., Hajiboland, R., Kump, P., Pongrac, P., Kaulich, B., Gianoncelli, A., Babin, V., Barceló, J., Regvar, M. & Poschenrieder, C. (2011). *J. Plant Res.* **124**, 165–172.
Vila-Comamala, J., Jefimovs, K., Raabe, J., Pilvi, T., Fink, R. H., Senoner, M., Maassdorf, A., Ritala, M. & David, C. (2009). *Ultramicroscopy*, **109**, 1360–1364.
Vogt, S., Chapman, H. N., Jacobsen, C. & Medenwaldt, R. (2001). *Ultramicroscopy*, **87**, 25–44.
Vogt, U., Lindblom, M., Charalambous, P., Kaulich, B. & Wilhein, T. (2006). *Opt. Lett.* **31**, 1465–1467.
Wilhein, T., Kaulich, B., Di Fabrizio, E., Romanato, F., Cabrini, S. & Susini, J. (2001). *Appl. Phys. Lett.* **78**, 2082–2084.
Winn, B., Ade, H., Buckley, C., Feser, M., Howells, M., Hulbert, S., Jacobsen, C., Kaznacheyev, K., Kirz, J., Osanna, A., Maser, J., McNulty, I., Miao, J., Oversluizen, T., Spector, S., Sullivan, B., Wang, Y., Wirick, S. & Zhang, H. (2000). *J. Synchrotron Rad.* **7**, 395–404.
Wunderer, C. R., Marras, A., Bayer, M., Correa, J., Göttlicher, P., Lange, S., Shevyakov, I., Smoljanin, S., Tennert, Viti, M., Xia, Q., Zimmer, M., Das, D., Guerrini, N., Marsh, B., Sedgwick, I., Turchetta, R., Cautero, G., Gianoncelli, A., Giuressi, D., Menk, R., Stebel, L., Yousef, H., Marchal, J., Rees, N., Tartoni, N. & Graafsma, H. (2015). *J. Instrum.* **10**, C02008.
Yun, W., Lai, B., Cai, Z., Maser, J., Legnini, D., Gluskin, E., Chen, Z., Krasnoperova, A. A., Vladimirsky, Y., Cerrina, F., Di Fabrizio, E. & Gentili, M. (1999). *Rev. Sci. Instrum.* **70**, 2238–2241.
Zangrando, M., Zacchigna, M., Finazzi, M., Cocco, D., Rochow, R. & Parmigiani, F. (2004). *Rev. Sci. Instrum.* **75**, 31–36.
Zeitler, E. & Thomson, M. G. R. (1970). *Optik (Stuttgart)*, **31**, 25.